computation

MDPI

Article

Effect of Spraying Characteristics on Combustion of Red Liquor—Virtual Experiments Using CFD Simulation

Barbara D. Weiß [1,*], Eva-Maria Wartha [1], Christian Jordan [1], Thomas Ladinek [2], Bahram Haddadi [3] and Michael Harasek [1]

[1] Institute of Chemical, Environmental & Bioscience Engineering, TU Wien, Getreidemarkt 9, 1060 Vienna, Austria
[2] Sappi Austria Produktions-GmbH & Co. KG, Sappi Europe, Brucker Straße 21, 8101 Gratkorn, Austria
[3] Competence Center CHASE GmbH, Ghegastraße 3, 1030 Vienna, Austria
* Correspondence: barbara.weiss@tuwien.ac.at

Abstract

Red liquor combustion is a crucial step in the chemical recovery process in the pulp and paper industry and has two main functions: recovering MgO and SO_2 from magnesium bisulfite spent liquor and generating steam as a heat source for further usage. This research aims to analyze how different red liquor spraying characteristics affect combustion time, guiding recommendations for optimal spraying characteristics to achieve faster combustion using computational fluid dynamics (CFD). Red liquor combustion is simulated in the open-source environment OpenFOAM®, employing Eulerian–Lagrangian coupling simulations, treating red liquor droplets as Lagrangian particles. One-step devolatilization and combustion kinetics are derived from performed non-isothermal thermogravimetric analyses (TGA) and implemented into the model. An industrial red liquor combustion vessel served as a reference case. Through virtual experiments, we explore the impact of spray angle (15° and 30°), droplet size (2 mm and 3 mm), and spray type (fullcone vs. hollowcone) on combustion time. The performed simulations indicate that the combustion time can be reduced by approximately 30% by reducing the characteristic particle diameter from 3 mm to 2 mm. Furthermore, hollowcone spraying revealed faster combustion times than fullcone spraying. The fastest combustion time was achieved with a characteristic particle size of 2 mm, a spraying angle of 30°, and using a hollowcone spray type.

Keywords: fuel spraying; Lagrangian particle combustion; pulping liquor; recovery boiler; CFD simulation

Academic Editor: Ali Cemal Benim

Received: 21 April 2026
Revised: 19 May 2026
Accepted: 29 May 2026
Published: 2 June 2026

1. Introduction

The combustion of spent pulping liquor is a crucial part of the chemical recovery process in the pulp and paper industry. Among the sulfite-based pulping processes, magnesium bisulfite pulping is dominant due to its potential for almost complete chemical recovery [1]. During the combustion of magnesium bisulfite spent liquor, also called red liquor, MgO is recovered in the ash. Sulfur is mainly oxidized to SO_2, resulting in a SO_2-loaded combustion gas. The recovered MgO is washed and hydrated to $Mg(OH)_2$, which subsequently serves as an absorbent in a multistage SO_2 absorption process. During the absorption, SO_2 and $Mg(OH)_2$ form magnesium bisulfite, which can then be reintroduced as pulping liquor. Such chemical recovery minimizes the usage of fresh chemicals, thus

lowering the process's environmental footprint. However, the combustion of red liquor affects the chemical usage in the pulping process beyond the chemical recovery, as ineffective combustion leads to soot formation, which is carried through the whole chemical recovery process to the pulp, leading to the coloration of the pulp, thus causing an increased demand for bleaching agents. Figure 1 visualizes the journey of soot in chemical recovery in a simplified manner.

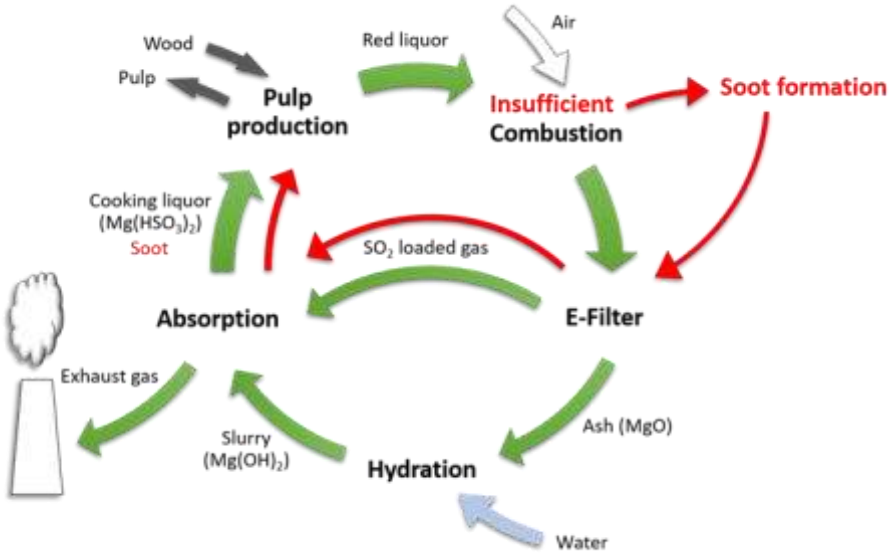

Figure 1. Simplified scheme of the chemical recovery when soot forms during combustion.

Improving combustion has, therefore, a dual effect: it enhances the efficiency of the pulp recovery process and reduces the necessity of bleaching agents, resulting in an overall reduced environmental footprint and increased economic viability.

Due to its large inorganic content and high water content, spent pulping liquor has a very low heating value of 12–15 MJ/kg compared to other industrial fuels (e.g., heating oil: 41 MJ/kg), making its effective combustion challenging [2]. Red liquor is sprayed into the furnace with a water content of around 30 to 40 wt%. The spraying characteristics of the fuel highly influence the combustion efficiency inside the furnace. Optimizing the spraying behavior in a furnace can significantly enhance the combustion efficiency of existing furnaces without the necessity of redesigning the furnace. This study aims to investigate the effect of spraying characteristics on the combustion speed of fuel droplets inside an industrial-scale combustion vessel via computational fluid dynamics (CFD) simulations. While the used reference case is tailored to an industrial-scale combustion vessel of red liquor, the simulation approach and the results can also be expanded to other fuels with high water content and large droplet spraying (mm).

A great part of research focuses on studying the spraying and its influence on the combustion of very fine droplets (µm) [3–5]. Droplet sizes for the combustion of spent pulping liquor are typically in the range of mm. Although the pulp and paper industry accounts for 1.1% of direct global industrial combustion and process CO_2 emissions [6,7], and the combustion of spent pulping liquor poses a particular challenge due to its mentioned characteristics, academic research on optimizing the design of spent pulping liquor combustion furnaces and their fuel spraying is scarce. Horton et al. studied in 1992 the effect of spraying on the combustion of black liquor using CFD simulation [8]. Laitinen et al. performed CFD simulations of a black liquor boiler to study the dispersion of sprayed droplets and the secondary air supply system without implementing combustion models

[9]. Black liquor refers to the liquor from an alkaline sulfate-based pulping process (Kraft process), while red liquor refers to the liquor from sulfite-based pulp processes. However, to our knowledge, no study has focused on simulating the combustion of red liquor and deriving recommendations on improved fuel spraying for such challenging fuels, making this a novel study in the field of applied CFD.

In this study, we apply one-step combustion models for the combustion of red liquor and perform a comparative study on the effect of spraying behavior on droplet combustion time. To model the combustion, we follow an Eulerian–Lagrangian approach, which allows us to track the fuel droplets inside the furnace. A two-way coupling enables the exchange of momentum, energy, and mass between the discrete fuel droplets and the continuous phase. The Eulerian–Lagrangian method is a widely recognized approach to describe liquid fuel spraying [10].

The CFD simulation setup allows us to run experiments in a virtual environment. By varying spraying characteristics such as spraying angle, droplet size, and spray type, we are predicting which factor is most influential in speeding up combustion inside the vessel and which spraying behavior is the most promising regarding combustion time.

2. Materials and Methods

In this chapter, we introduce the methods used for our study. Section 2.1 provides the governing equations of the applied Eulerian–Lagrangian approach. In Section 2.2, we introduce the phase change and reaction models used. Finally, we present the simulation setup on which the developed workflow was tested, including the simulation geometry, the computational mesh, and the boundary conditions. This chapter closes by summarizing the performed virtual experiments in Section 2.4.

2.1. Computational Fluid Dynamics (CFD)

The simulations are performed in the open-source simulation environment OpenFOAM® version 9 using the solver reactingFoam. The combustion vessel operates in stable conditions, allowing the simulations to be performed in a steady state. Figure 2 visualizes the concept of the applied Eulerian–Lagrangian approach. Although describing Lagrangian particles can be computationally intensive, this method's advantage lies in its ability to track specific properties of individual particles.

The gas phase is described as Eulerian phase. The liquid fuel droplets are modeled as wet solid point centers of mass with constant volume and described as Lagrangian particles. The coupling between the Eulerian phase and the Lagrangian particles is realized as a two-way coupling. The influence of the fuel droplets (Lagrangian particles) on the gas phase (Eulerian phase) is modeled employing source terms. The influence of the gas phase on the fuel droplets is modeled using submodels. To save computational time, particles are grouped into representative parcels, each comprising numerous particles with the same characteristics that are tracked and solved together. In this study, 100 particles are grouped into one parcel.

https://doi.org/10.3390/computation14060130

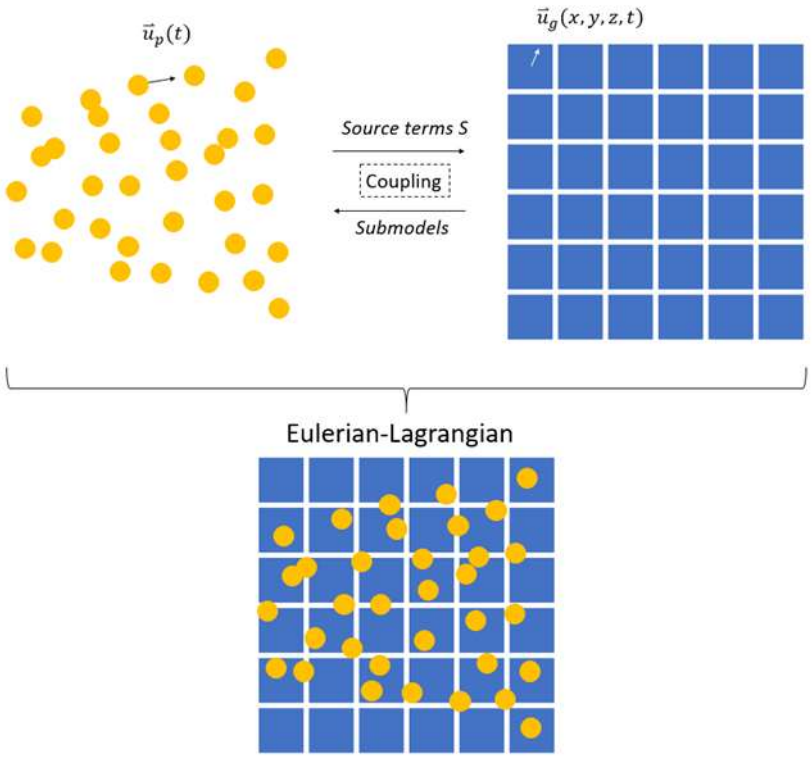

Figure 2. (**Top left**): Lagrangian particles; (**top right**): Eulerian flow; (**bottom**): Eulerian–Lagrangian approach (visualization inspired by Hirche et al. [11]).

The $k-\varepsilon$ model is used to account for turbulence with the default model coefficients [12,13]. The $k-\varepsilon$ model is commonly used in the simulation of industrial furnaces in OpenFOAM® [14,15]. k represents the turbulent kinetic energy, and ε the eddy dissipation rate. The eddy dissipation rate gives the rate at which turbulent kinetic energy transforms into internal thermal energy due to viscous effects. Radiation was calculated using the P1 model, a commonly used radiation approximation for particle combustion processes, as implemented in OpenFOAM® [16]. The following describes the modeling of the Eulerian flow and the Lagrangian particles.

2.1.1. Eulerian Flow

The Eulerian flow is described employing the continuity equation, the momentum equation, the energy equation, and the species equation (Equations (1)–(3)).

The continuity equation with S_m being the source term for mass reads

$$\frac{\partial \rho_g}{\partial t} + \nabla \cdot \left(\rho_g U_g\right) = S_m \tag{1}$$

where ρ_g is the density and U_g is the velocity. S_m results from reaction and phase change.

The momentum equation for compressible fluids reads

$$\frac{\partial \left(\rho_g U_g\right)}{\partial t} + \nabla \cdot \left(\rho_g U_g U_g\right) - \nabla \cdot \left(\tau_g\right) = -\nabla \mathrm{p} + \rho_g \mathrm{g} + S_u \tag{2}$$

The equation includes viscous force with τ_g being the stress tensor. S_u describes the momentum source term resulting from interaction with the Lagrangian particles.

The energy equation includes diffusion with α_{eff} being the effective thermal diffusivity and reads

$$\frac{\partial (\rho_g (h+K))}{\partial t} + \nabla \cdot \left(\rho_g U_g (h+K)\right) - \nabla \cdot \left(\alpha_{eff} \nabla h\right) = \nabla \mathrm{p} + \rho_g U_g \cdot \mathrm{g} + S_h \tag{3}$$

h is enthalpy, and K the kinetic energy. S_h is the energy source term resulting from the exchange with the Lagrangian particles.

To describe the multi-component nature of the flow, the species equation is applied with S_i being the species source term resulting from reaction and phase change. The species equation reads

$$\frac{\partial \rho_g Y_i}{\partial t} + \nabla \cdot \left(\rho_g U_g Y_i\right) - \nabla \cdot \left(\frac{\mu_{eff}}{Sc} \nabla (\rho_g Y_i)\right) = S_i \tag{4}$$

Y_i describes the mass fraction for species i, μ_{eff} the effective viscosity for species transport, and Sc the Schmidt number. The last term represents the diffusion of the species' mass fraction.

2.1.2. Lagrangian Particles

Newton's second law of motion describes the movement of the Lagrangian particles. Drag force F_D, gravitational force F_g and lift force F_L are acting on the particle, leading to the following equation:

$$\frac{d}{dt}\left(m_p U_p\right) = F_D + F_g + F_L \tag{5}$$

where m_p is the particle mass and U_p the particle velocity.

The drag force is calculated with the sphereDrag model from the OpenFOAM® library:

$$F_D = \frac{m_p}{U_g} \frac{3}{4} \frac{\mu_g C_D Re_p}{\rho_P d_p^2} \tag{6}$$

μ_g is the dynamic viscosity, U_g is the velocity of the carrier (gas phase) at the cell-occupying particle, ρ_P is the particle mass density and d_P is the particle diameter. The particle drag coefficient C_D is based on the empirical expression by Putnam [17]:

$$C_D = \frac{24}{Re_p}\left(1 + \frac{1}{6} {Re_p}^{\frac{2}{3}}\right) \text{ if } Re_p \leq 1000 \text{ and } C_D = 0.424 \text{ if } Re_p > 1000 \tag{7}$$

The lift force is calculated following

$$F_L = m_p \frac{\rho_g \frac{3}{2\pi\sqrt{Re_w}} C_L}{\rho_P} \left(U_g - U_p\right) \times \omega \tag{8}$$

where $\omega = \nabla \times U$ is the vorticity of the gas at particle location and $Re_w = \frac{\rho_g d_p^2 |\omega|}{\mu_g}$. The lift coefficient C_L is based on the Saffman–Mei expression [18,19]:

$$C_L = 6.46\left(1 - 0.3314\sqrt{\frac{1}{2}\frac{Re_w}{Re_p}}\right) e^{-0.1 Re_p} + 0.3314\sqrt{\frac{1}{2}\frac{Re_w}{Re_p}} \text{ if } Re_p < 40 \text{ and}$$
$$C_L = 6.46 \cdot 0.0524\sqrt{\frac{1}{2} Re_w} \text{ if } Re_p \geq 40 \tag{9}$$

A stochastic dispersion model is applied to account for perturbation of a particle due to turbulence [20]. The particle is perturbed by turbulence if the timestep is smaller than τ_{tur}:

$$\tau_{turb} = \min\left(\frac{k}{\varepsilon}, 0.16432 \frac{k^{1.5}}{\varepsilon U_{rel}}\right) \tag{10}$$

where

$$U_{rel} = \left|U_p - U_g - U_{turb}\right| \tag{11}$$

With U_p being the particle velocity, U_g the gas phase velocity and U_{turb} the turbulent velocity. The velocity undergoes perturbation in a random direction:

$$U_{turb} = \sqrt{\frac{2k}{3}}|N|d_v \tag{12}$$

where N is a random normal with mean 0 and standard deviation 1, and d_v is a vector with $[a\cos(\theta), a\sin(\theta), u]$. a is random between 0 and 1, u is random between −1 and 1, and θ is random between 0 and 2π. The model is part of the standard OpenFOAM® library under the name StochasticDisperisionRAS.

The gas-particle heat transfer is modeled using the empirical Nusselt correlation by Ranz-Marshall [21]:

$$Nu = 2 + 0.6Re_p^{\frac{1}{2}}Pr^{\frac{1}{3}} \tag{13}$$

2.2. Phase Change and Reactions

Phase change and reaction models are implemented to model the combustion of red liquor. Drying, devolatilization, and char combustion are the three main stages of red liquor combustion [2]. The fourth stage is smelting of ash, which is a slow process and disregarded in the performed simulation due to the short residence time of the fuel droplets in the furnace. Red liquor combustion is a complex reaction system during which organic matter is burnt, and inorganic matter is recovered in the ash. In this study, a simplified combustion reaction system is implemented that summarizes the complex combustion system into four steps with two reactions:

1. Drying;
2. Devolatilization;
3. Volatile combustion in the gas phase:

$$C_xH_yO_zS_s + \left(x + \frac{y}{4} - \frac{z}{2} + s\right)O_2 \rightarrow \mathrm{x\ CO_2} + \frac{\mathrm{y}}{2}\ \mathrm{H_2O} + \mathrm{s\ SO_2} \tag{14}$$

4. Char combustion:

$$C + O_2 \rightarrow \mathrm{CO_2} \tag{15}$$

Figure 3 visualizes the combustion steps that are implemented in the simulations.

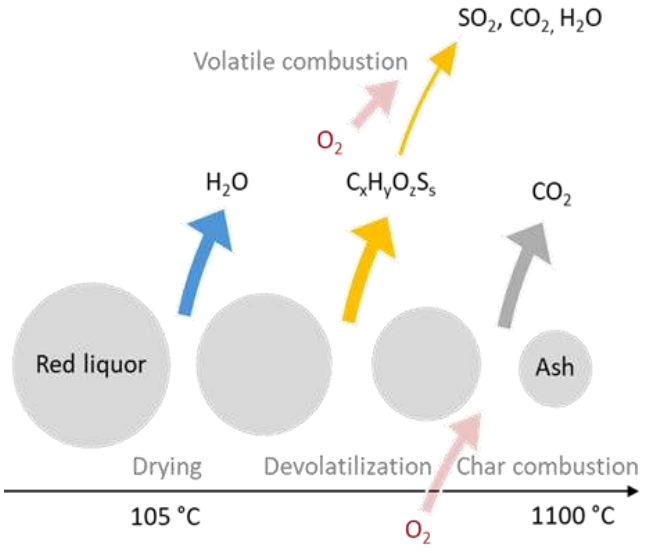

Figure 3. Visualization of implemented combustion steps.

The stoichiometry of the gas phase reaction can be derived from the known elemental composition of red liquor. While several studies in the literature study the kinetics of black liquor [22,23], the available studies on red liquor are scarce. The composition of red liquor, being highly specific, can introduce significant variations in the kinetics of reactions. Hence, we generated our own kinetics data tailored to our red liquor composition. For this purpose, thermogravimetric analyses were performed. The following section describes the conducted analyses and the implemented phase change and reaction models.

2.2.1. Thermogravimetric Analyses of Red Liquor

Non-isothermal thermogravimetric analyses (TGA) of red liquor were conducted to investigate its devolatilization and combustion behavior. The experiments were carried out using an STA 449 C Jupiter instrument manufactured by NETZSCH. TGA experiments were performed under two different gas environments: nitrogen (N_2) and an oxidizing environment containing 21 vol% oxygen (O_2). The sample was dried by holding the temperature at 105 °C for 100 min. After drying, the heating rate was set to 15 K/min. The sample was heated to 1100 °C. During the experiments, the weight of the sample was recorded. From the recorded data, various parameters describing the devolatilization and combustion behavior are derived:

- Temperature at which devolatilization starts (T_{Devol});
- Mass fraction of volatiles left when combustion starts (volatile residual coefficient);
- Kinetic data for devolatilization and char combustion.

Figure 4 shows the temperature and mass loss referred to the dry basis over time from the TGA results.

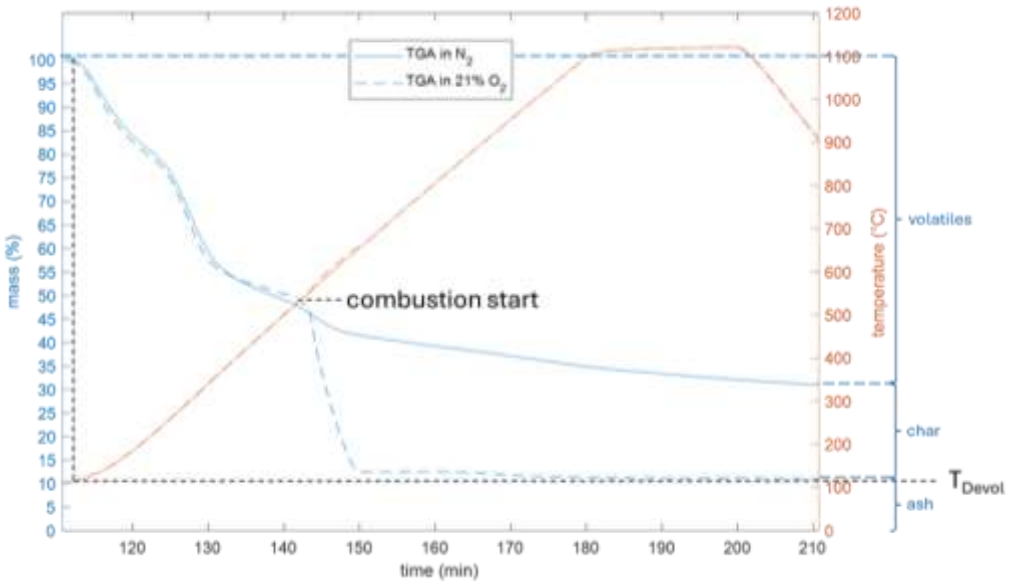

Figure 4. TGA result: temperature and mass loss (wt% dry mass) over time in N_2 and oxidizing environment after 100 min of drying.

The ash, char, and volatile content align with the elemental composition as detailed in Section 2.4. Devolatilization initiates at 115 °C (T_{Devol}). Combustion initiates with a volatile residual coefficient of 0.254. The devolatilization process reveals three distinct zones, suggesting a division between light and heavy volatiles. However, for simplicity, we have aggregated the volatiles into a single group in this study.

To obtain kinetic data for devolatilization and char combustion, the Arrhenius equation, which relates the rate constant of a chemical reaction to the temperature and activation energy, was utilized:

$$k_{kin} = Ae^{-\frac{E}{RT}} \quad (16)$$

with A being the pre-exponential factor, E the activation energy, R the universal gas constant, and T the absolute temperature. Non-linear least squares regression was employed to fit the Arrhenius equation to the experimental data. This fitting process yielded the pre-exponential factor (A) and the activation energy (E) for both devolatilization and carbon combustion. Finally, the quality of the fit was assessed by comparing the model predictions based on the optimized parameters with the experimental data.

In our study, we opted for this simplified approach to determine the kinetics of our red liquor system instead of more sophisticated methods, such as the Ozawa–Flynn–Wall model that requires TGA with at least three different heating rates. While these advanced techniques offer comprehensive insights into the kinetics of reactions, our primary goal was to obtain a preliminary indication of the kinetics rather than delve deeply into kinetic analysis. This approach provided us with a foundational understanding of the kinetics, setting a solid groundwork for future in-depth studies if necessary. Table 1 summarizes the results for E and A from the data fitting.

Table 1. Activation energy E and pre-exponential factor A from data fitting.

	E (J/kmol)	A (1/s)
Devolatilization	3.54×10^6	3.16
Char combustion	1.17×10^7	44.98

Figure 5 shows the model predictions for the devolatilization based on the values from Table 1 and the experimental data.

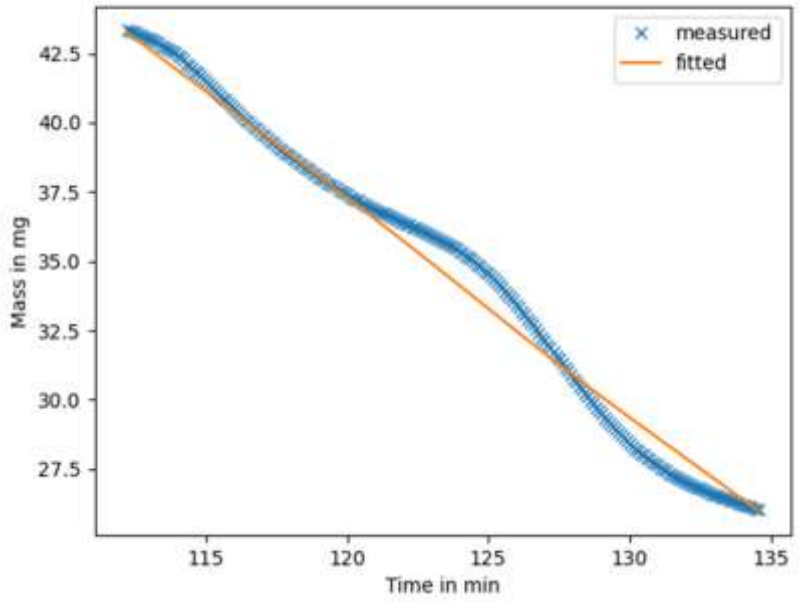

Figure 5. Model prediction for grouped volatiles and experimental mass loss over time during devolatilization (t = 112–135 min).

Figure 6 shows the model predictions for the char combustion based on the values from Table 1 and the experimental data.

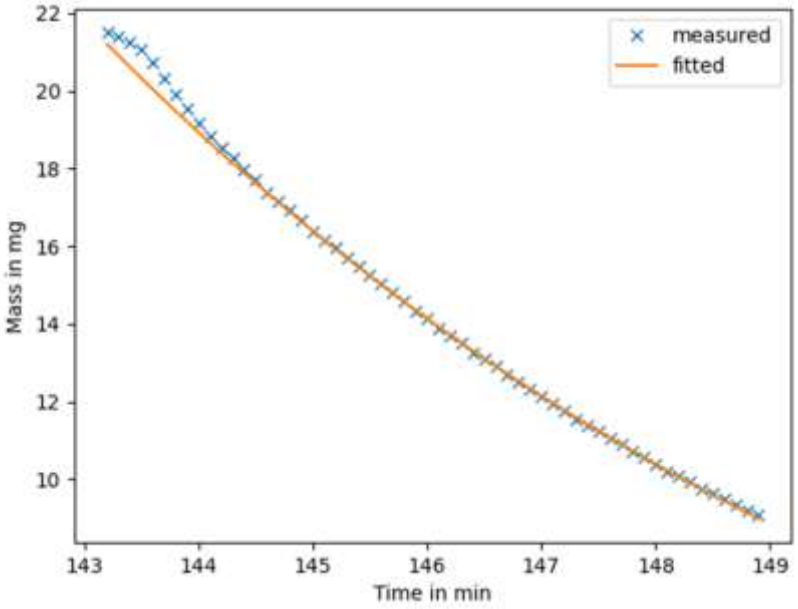

Figure 6. Model prediction and experimental mass loss over time during char combustion (t = 143.2 min–149 min).

2.2.2. Phase Change and Reaction Models

The following describes the applied phase change and reaction models, including drying of fuel droplets, devolatilization, gas phase combustion, and solid char combustion.

Drying of Fuel Droplets

Drying of the particle is calculated using the Spalding evaporation model [24]:

$$\frac{dm_{H2O}}{dt} = -\pi d_p Sh \rho_g D_{H_2O} ln\left(1 + \frac{Y_{H_2O,F} - Y_{H_2O,\infty}}{1 - Y_{H_2O,F}}\right) \quad (17)$$

with D_{H_2O} being the diffusion coefficient and Sh the Sherwood number, which describes the ratio of convective to diffusive mass transport. $Y_{H_2O,F}$ represents the mass fraction of evaporated water in the film surrounding the droplet and $Y_{H_2O,\infty}$ in the far field. A detailed description of the model can be found in [25]. If the saturation pressure is greater than 99.9% of the critical pressure of water, drying is calculated as flash boiling based on the model by Zuo et al. [26].

Devolatilization

$$\frac{dm}{dt} = k_{kin} \cdot m \quad (18)$$

The kinetic rate k_{kin} is calculated following Arrhenius (Equation (16)). The activation energy E and the pre-exponential factor A are given in Table 1.

We use a pseudo-species $C_xH_yO_zS_s$ to represent the volatile components that combust, as described in Equation (14). Because there are no thermophysical properties for such a pseudo-species, we calculate the molecular weight according to the reaction equation and otherwise use CH_4 properties as an estimation. To close the overall energy balance of red liquor conversion (dry heating value of 13.4 MJ/kg), we use the latent heat of devolatilization and calculated it to be 8.9 MJ/kg; 20% of the enthalpy is retained by the particle due to surface reactions.

Gas Phase Combustion

The combustion of volatiles in the gas phase reads

$$vol = C_x H_y O_z S_s$$
$$vol + 2.5245\ O_2 \rightarrow 2.202\ CO_2 + 2.853\ H_2O + 0.507\ SO_2 \quad (19)$$

The gas phase combustion is modeled using the Eddy Dissipation Diffusion Model [27]. The use of this model assumes that, once volatiles are released, their oxidation occurs in a highly turbulent reacting flow where the characteristic mixing time scales are significantly shorter than the global reaction time scales. This Turbulence–Chemistry Interaction Model is commonly used to predict the combustion behavior in turbulent flows [28]. The model does not use kinetic data. The time scale is determined by the minimum turbulence and diffusion time scales. The turbulence mixing time scale is taken from the turbulence model ($k - \varepsilon$). The diffusion time scale describes the volatile–oxygen mixing in laminar regions:

$$w_{vol} = \frac{\rho}{C} \min\left(Y_{vol}, \frac{Y_{O_2}}{2.5245}\right) \max\left(t_{diff}, t_{turb}\right) \quad (20)$$

$$t_{diff} = AB \frac{\nu_{eff}}{(\Delta t)^2} \quad (21)$$

$$t_{turb} = C_{EDC} \frac{\epsilon}{k} \quad (22)$$

with Y_{vol} being the volatile mass fraction, Y_{O_2} the oxygen mass fraction, and 2.5245 the stoichiometric oxygen to volatile ratio. It needs to be noted that, while this model is commonly applied in turbulent flows, it may overpredict reaction rates in regions where the flow is locally mixing-limited. As described in Section Devolatilization, the thermophysical properties of the volatiles were estimated using properties of CH_4. This approximation may lead to an overestimation of volatile diffusivity and turbulent mixing, potentially resulting in earlier gas-phase combustion, which needs to be considered when interpreting local gas concentration and temperature fields. Nevertheless, the overall combustion process investigated in this study is predominantly limited by the comparatively slow Arrhenius-based devolatilization kinetics of the particles. Therefore, the approximation is not expected to significantly influence the predicted particle combustion times, although local gas-phase combustion characteristics and temperature distributions may be affected.

Carbon Combustion

The char combustion

$$C + O_2 = CO_2 \quad (23)$$

is calculated following the single kinetic rate model

$$\frac{dm_{char}}{dt} = k_{kin}\, m \quad (24)$$

The kinetic rate k_{kin} is calculated following Arrhenius (Equation (16)). The activation energy E and the pre-exponential factor A are given in Table 1.

2.3. Simulation Setup

The simulation setup was based on an industrial red liquor combustion vessel as a reference case. The following describes the simulation geometry, the computational mesh, and the applied boundary conditions.

2.3.1. Simulation Geometry

Figure 7 shows the 3D geometry of the combustion vessel with its inlets and outlets.

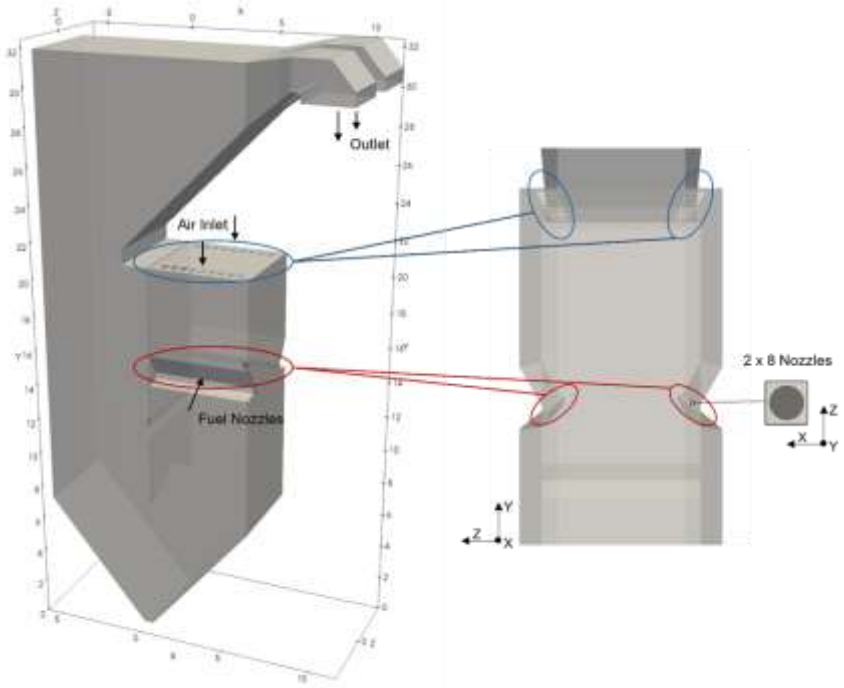

Figure 7. Combustion vessel with inlets and outlets (dimensional grid in m).

The combustion air enters through 18 square openings from the top, while the fuel enters through 16 nozzles modeled as round openings with a diameter of 27 mm. The combustion zone is lined with refractory material, simulated as adiabatic walls. The vessel is simulated until the outlet shown in Figure 1, which is situated before the gas cleaning units. As the combustion gas travels towards the outlet, it heats steam through tube bundle heat exchangers, modeled as anisotropic porous zones with a heat sink (Figure 8).

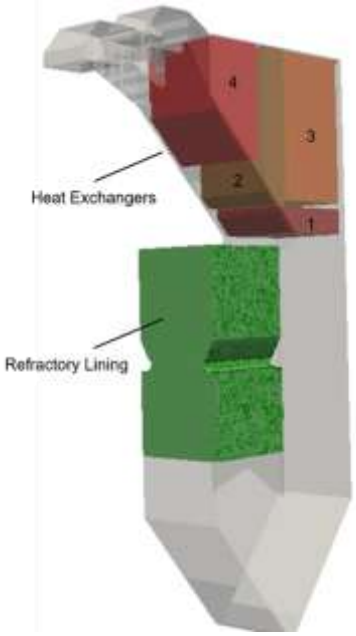

Figure 8. Heat exchangers 1 to 4 in red and brown and refractory lining zone in green.

The porosity accounts for pressure loss, and the heat sink for the heat transfer. For each heat exchanger, the porosity $f_{x,y,z}$ is calculated in x, y, and z directions as follows:

$$f_{x,y,z} = \frac{A_{void}}{A_{total}} \tag{25}$$

with A_{void} being the void area and A_{total} the total area. The pressure loss Δp is calculated according to the Darcy–Forchheimer law

$$\Delta p = -\left(\mu D + \frac{\rho |U|}{2} F\right) U \tag{26}$$

with μ being the dynamic viscosity, ρ the density of the fluid, and U the velocity of the fluid. D and F are the Darcy and the Forchheimer coefficients, respectively. Assuming the heat bundles are perforated plates, Idelchik's equation for perforated plates is applied [29]:

$$D = 0 \text{ and}$$

$$F_{x,y,z} = \frac{\left(0.707\left(1 - f_{x,y,z}\right)^{0.375} + 1 - f_{x,y,z}\right)^2}{{f_{x,y,z}}^2} \tag{27}$$

Table 2 summarizes the applied Forchheimer coefficients F.

Table 2. Forchheimer coefficients F for heat exchangers 1 to 4 in 1/m.

	1	**2**	**3**	**4**
F_x	0.1654	0.8742	0.1654	0.8742
F_y	0.1654	0.8742	0.1402	0.6295
F_z	3.3624	3.3449	1.3337	1.8810

The heat transfer over the heat exchangers is known from standard operation of the vessel. Table 3 summarizes the applied heat loss over the heat exchangers. The heat sink is applied as a heat source to the defined porous zones.

Table 3. Heat sink of heat exchangers 1 to 4 in MJ.

1	**2**	**3**	**4**
2440	1850	1030	1540

2.3.2. Computational Mesh

To perform the CFD simulation, the domain of interest is discretized into a predominantly hexahedral mesh using snappyHexMesh in OpenFOAM®. The domain is divided into four zones with different refinement levels to ensure reasonable computational times while having a fine enough computational grid (Figure 9).

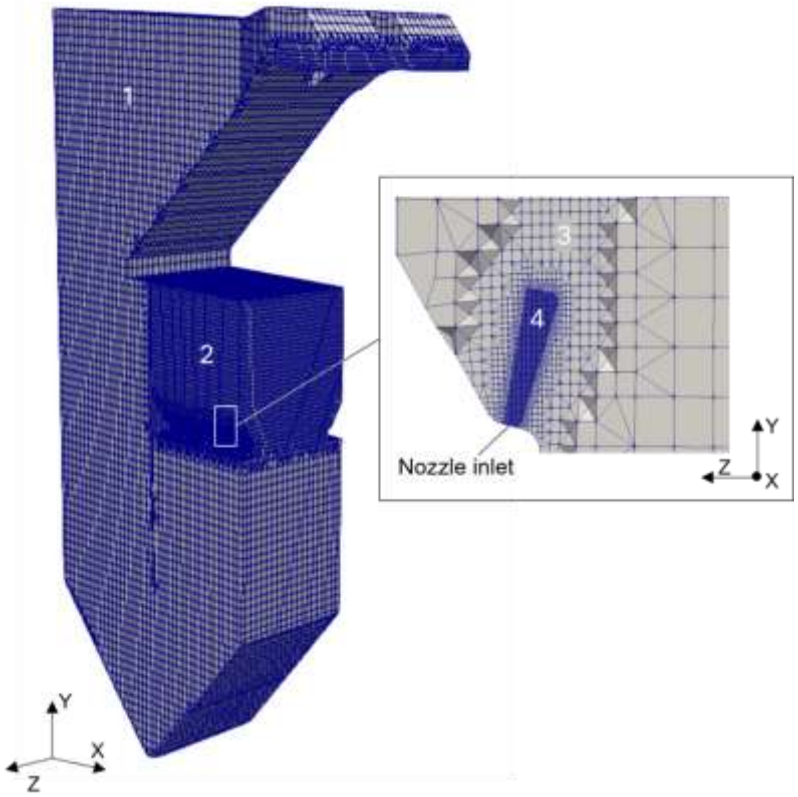

Figure 9. Calculation mesh with four different refinement levels ((**left**): overall combustion vessel, (**right)**: nozzle inlet area).

The mesh has 867,000 cells and is divided into four regions with different refinement levels (see Figure 9). The mesh has a maximum aspect ratio of 7.7, maximum non-orthogonality of 59, and maximum skewness of 2.3.

The mesh size of mesh region 4, which is close to the nozzle inlet, is set to meet two conditions: First, the cell size is greater than the size of the fuel droplets (characteristic droplet sizes are 2 to 3 mm), a requirement to track the Lagrangian particles correctly (see Section 2.1). Second, the cell size is small enough to correctly predict the velocity field of the spraying. To determine which cell size meets the second condition, the velocity field of the spraying was calculated with different cell sizes and compared to literature values. Figure 10 shows the relative velocity along the centerline (centerline velocity Uc/maximum velocity at nozzle exit Um) of the spraying calculated with different cell sizes compared to data from Mi et al. [30].

Close to the nozzle, the velocity is predicted best by applying a cell size of 2.3 mm. Close to the nozzle, the velocity is underestimated when applying a cell size of 5.4 mm. However, 20 cm from the nozzle (x/De = 7), the velocity is predicted best when applying a cell size of 5.4 mm. The combination of two cell sizes, 2.3 mm close to the nozzle and 5.4 mm further from the nozzle, predicts the velocity best. However, looking at the 15° line of the nozzle spraying instead of the centerline, both meshes, the optimized mesh, combining the two cell sizes 2.3 and 5.4 mm, and the 5.4 mm mesh, are predicting a similar velocity. To ensure meeting the condition that the cell size is greater than the size of the fuel droplets, and following the observations made through the mesh study, a cell size of 5.4 mm was chosen for the simulation.

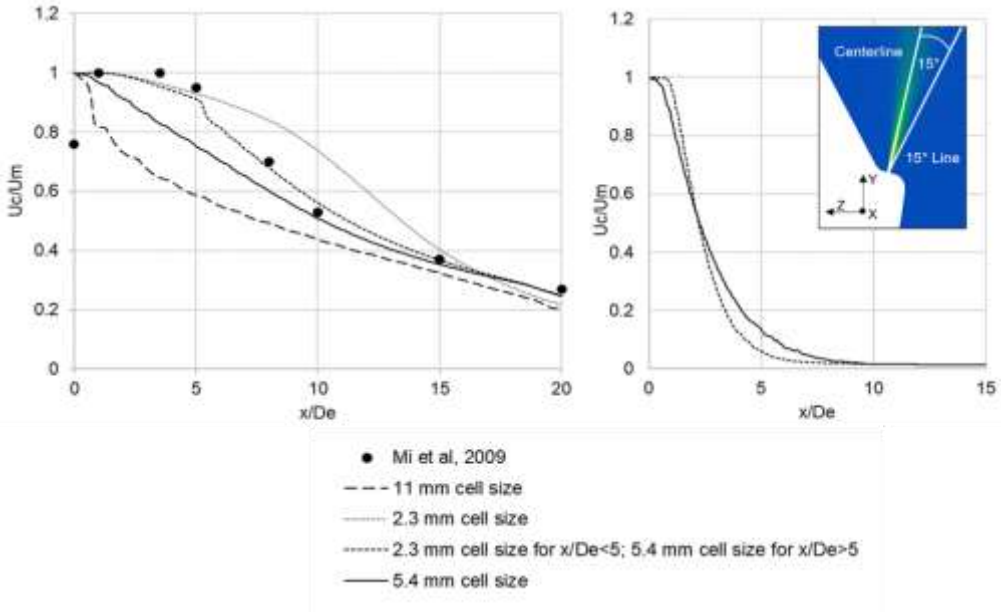

Figure 10. Simulation results vs literature values from Mi et al. [30] (**left**): Relative velocity along the center line, (**right**): relative velocity along 15° line; (x: distance from the nozzle; De: nozzle diameter).

Table 4 summarizes the cell average volumes of the different refinement levels of the final mesh.

Table 4. Cell volume of different refinement regions shown in Figure 9.

Refinement Region	1	2	3	4
Cell Volume (m^3)	4.601×10^{-4}	1.150×10^{-4}	7.189×10^{-6}	1.123×10^{-7}
Characteristic Cell Length (mm)	86.4	43.2	21.6	5.4

2.3.3. Boundary Conditions and Evaluation

The applied boundary conditions are based on normal operation conditions of the industrial reference combustion vessel. The red liquor has a water content of 38 wt%. The elemental composition on a dry basis is given in Table 5.

Table 5. Elemental composition of red liquor in wt% dry mass.

Ash	11.20
Char	21.80
Volatiles	67.00
C	39.5
H	3.9
S	10.9
O	34.5

A volumetric flow rate of 154 034 Nm^3/h at 383 °C is specified for the air inlet. The air composition comprises 76.52 wt% N_2, 23.4 wt% O_2, and 0.08 wt% CO_2. The red liquor spraying is a two-phase spraying with red liquor and water vapor. Red liquor is injected at a rate of 14.64 L/s with a density of 1302 kg/m^3, with a temperature of 106 °C. Simultaneously, water vapor is introduced at a rate of 2.82 kg/s, with a temperature of 162 °C. The particle injection in the simulations was modeled using the coneInjection model in OpenFOAM. Parcels, representing 100 particles, are injected with a constant mass flow of 1.188075 kg/s per nozzle at a constant velocity of 48.4 m/s. The radial mass distribution across the cone is uniform.

To assess the reliability of the simulation we compared our simulations to measurement data available from the industrial reference plant as well as to expectations derived from the literature. The assessment includes answering the following questions: Are the visualized results physically accurate and reasonable? Is the temperature inside the combustion vessel in agreement with measurement data? Is the gas composition at the outlet in agreement with measurement data? Is the combustion time in agreement with expectations based on literature values?

2.4. Virtual Experiments

The red liquor injection was simulated, varying three spraying parameters: spray type, spraying angle, and particle size. The spray type fullcone is a uniform spray across a cone of 27 mm; the spray type hollowcone is a uniform spray across a hollow cone with an outer diameter of 27 mm and an inner diameter of 22 mm. The particle-size distribution was modeled by drawing random samples from the Rosin–Rammler (Weibull) probability density function (PDF) as described in [31]. The shape parameter n was set to 3. The scale parameter λ, which represents the characteristic particle diameter, was varied. Figure 11 summarizes the varied parameters.

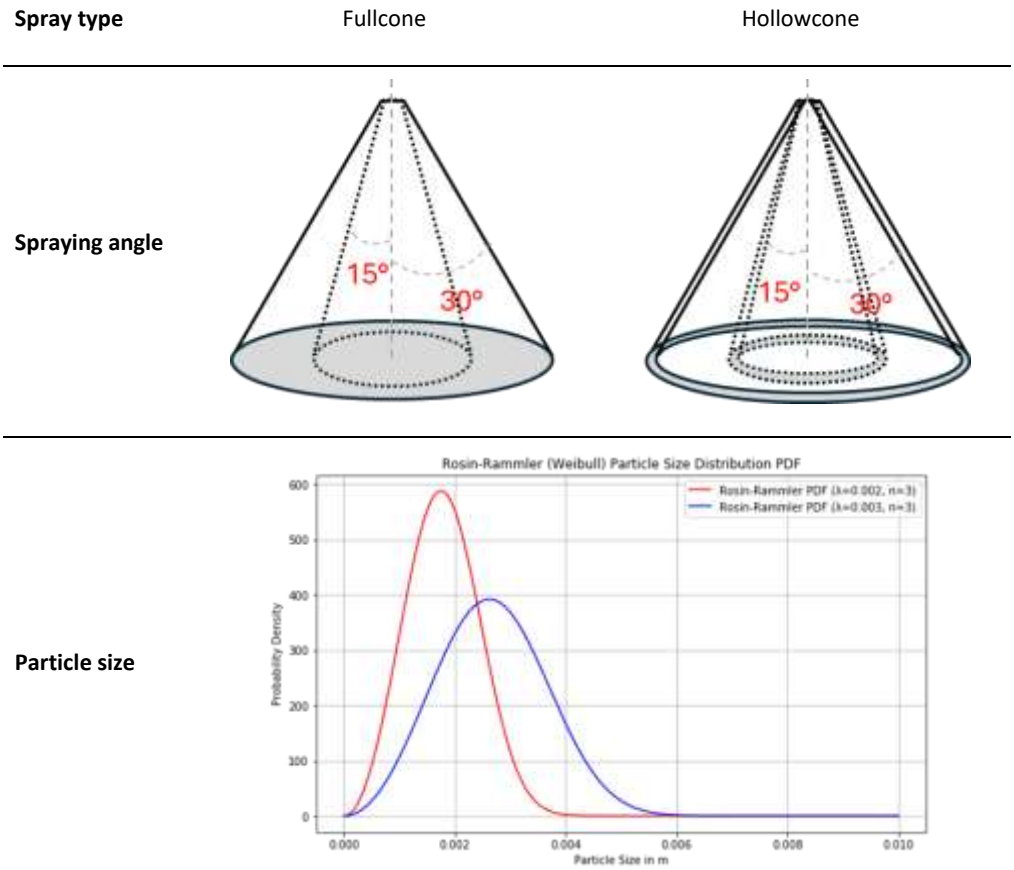

Figure 11. Varied parameters of virtual experiments.

The chosen parameters reflect typical spraying characteristics of industrial red liquor spraying. A characteristic diameter of 2–4 mm is reported for black liquor [2,32]. Table 6 summarizes the virtual experiments conducted in this study.

Table 6. Parameter setting in virtual experiments.

	Particle Size λ (mm)	Spraying Angle in (°)	Spray Type
Experiment #1	2	30	Hollowcone
Experiment #2	2	15	Hollowcone
Experiment #3	3	30	Hollowcone
Experiment #4	3	15	Hollowcone
Experiment #5	2	30	Fullcone
Experiment #6	2	15	Fullcone
Experiment #7	3	30	Fullcone
Experiment #8	3	15	Fullcone

3. Results and Discussion

The following presents the results of the simulations that were conducted. Firstly, the simulation case with a characteristic droplet diameter λ of 2 mm, a spraying angle of 30°, and the spray type hollowcone is examined in detail as a reference case to assess the accuracy of the simulations. Finally, the outcomes of the virtual experiments are presented.

3.1. Evaluation of Simulation Results

Figure 12 visualizes the Lagrangian particles colored based on their time inside the combustion vessel since injection and their ash content, representing simulation results.

The particles have a residence time of 8 to 10 s in the vessel and enter the cooling section of the heat exchangers after around 4 to 5 s. The increasing ash content of the visualized Lagrangian particles shows the progress of combustion as the particles travel through the combustion vessel. The results show that almost all particles have an ash content of 1 when reaching the vessel exit; only a few particles are not completely combusted. We can derive further insights into the reaction system inside the vessel by looking at the Eulerian field. Figure 13 shows the streamlines inside the vessel.

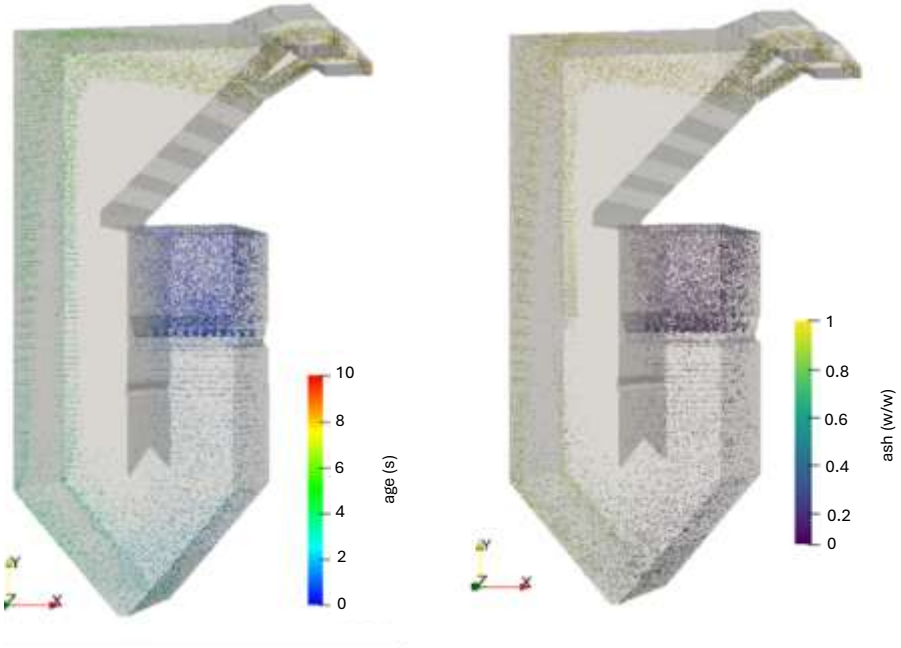

Figure 12. (**Left**): Lagrangian particles visualized scaled by factor 10, colored based on the age in s; (**right**): simulation results: Lagrangian particles visualized scaled by factor 10 colored based on the ash weight fraction.

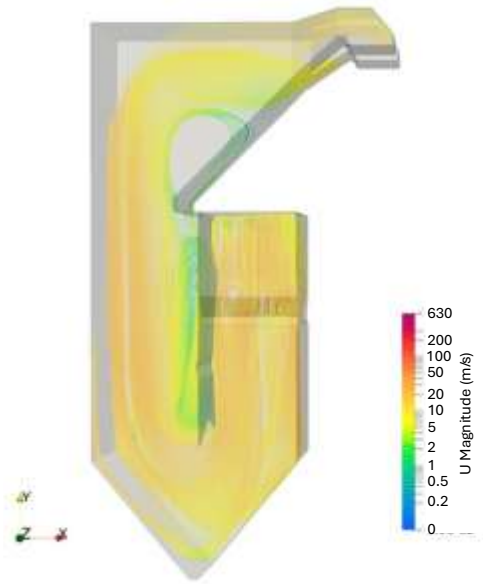

Figure 13. Calculated streamlines in the Eulerian field, colored based on the velocity in m/s.

The streamlines depict the gas flow through the furnace. Figure 14 shows the temperature along with the CO_2 content of the Eulerian field.

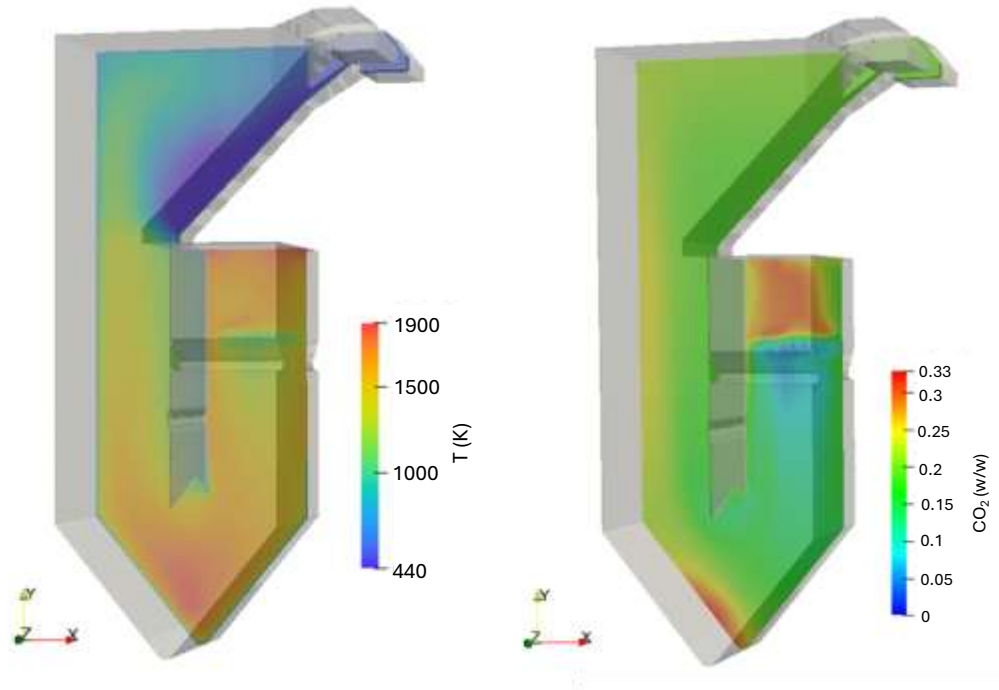

Figure 14. (**Left**): Simulation results for temperature in K in Eulerian field; (**right**): simulation results for CO_2 weight fraction in Eulerian field.

In the area of red liquor injection, the temperature drops due to water evaporation and the endothermic devolatilization. The temperature reaches a maximum of 1900 K inside the vessel due to exothermic combustion reactions and decreases over the heat exchangers due to their cooling effect. The increase in temperature in the area above fuel injection and at the vessel bottom can be traced to exothermic combustion reactions, which is confirmed by the increased CO_2 in those areas. The combustion above fuel injection can be attributed to

volatile combustion, while the combustion in the bottom area is due to char combustion. The volatile release and the volatile combustion can be seen in Figure 15.

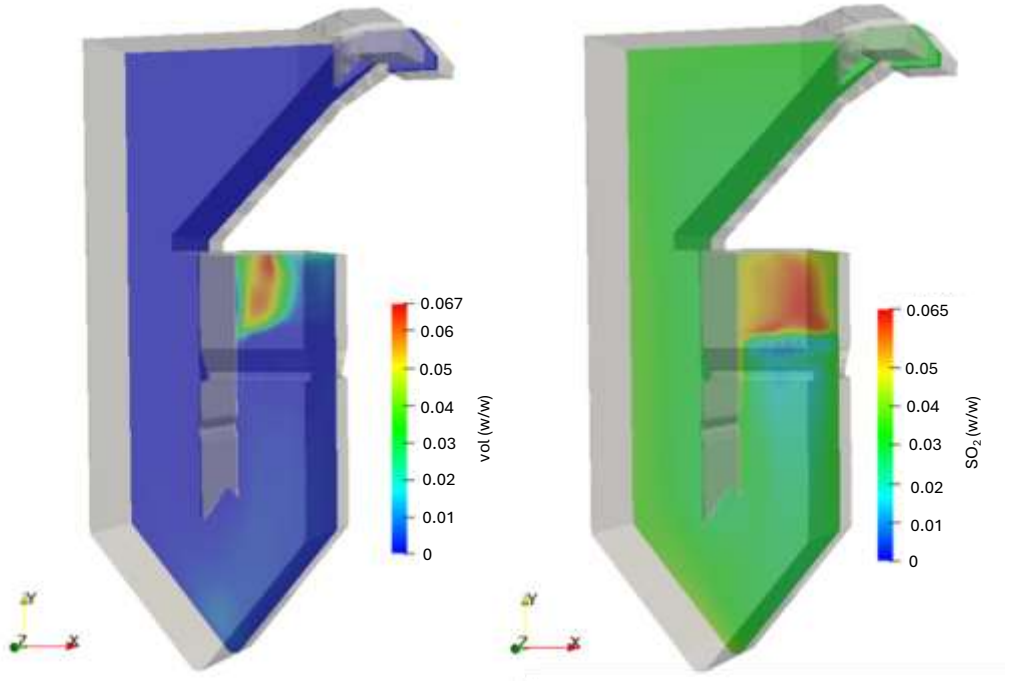

Figure 15. (**Left**): Simulation results for volatile weight fraction in Eulerian field; (**right**): simulation results for SO_2 weight fraction in Eulerian field.

The biggest volatile release is happening in the area above fuel injection, where the volatiles are also combusting, as the SO_2 increase in this area indicates.

Industrial data provide three temperature measurements on a plane inside the combustion vessel. The temperature profile at this plane was extracted from CFD simulations to evaluate the simulations (Figure 16).

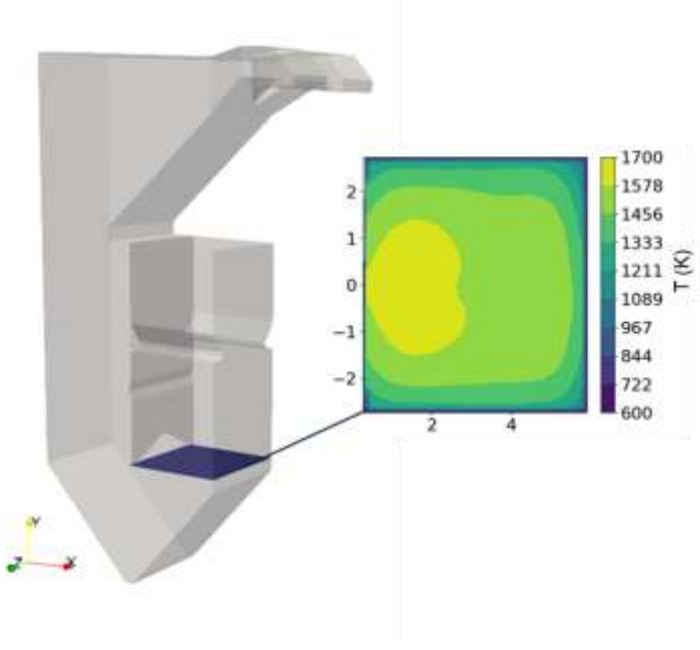

Figure 16. Combustion vessel with simulated temperature profile in K on plane highlighted in blue.

The temperature measurements at the plane are located approximately 0.5 m from the wall. The measured temperatures are in the range of 1465 K to 1485 K. The simulated temperatures closely match these measured values.

Further industrial data used to evaluate the performed simulations include the gas outlet composition. Table 7 summarizes the calculated and measured gas outlet composition. The deviation between calculation and measurement is given as

$$Deviation\ (\%) = \frac{x_{calculated} - x_{measured}}{x_{measured}} \cdot 100 \quad (28)$$

Table 7. Gas composition in vol% dry.

	Measurement with Standard Deviation s	Calculation	Deviation (%)
CO_2	17.4 (s:0.21)	17.89	3
O_2	2.29 (s:0.18)	4.65	103
SO_2	1.13 (s:0.02)	1.92	71

The calculated SO_2 content is 71% higher compared to the measurement. The simulation assumes that all the sulfur present in the fuel reacts to form SO_2. However, in reality, sulfur is partially recovered in the ash as $MgSO_4$, which explains the lower SO_2 content in the measurement. The CO_2 content has a deviation of 3% and is, therefore, in good agreement with the measurement. The calculated O_2 content is 103% higher than the measured one. Looking at the calculated gas composition over the outlet area, it is notable that the gas composition shows local differences across the outlet area (Figure 17).

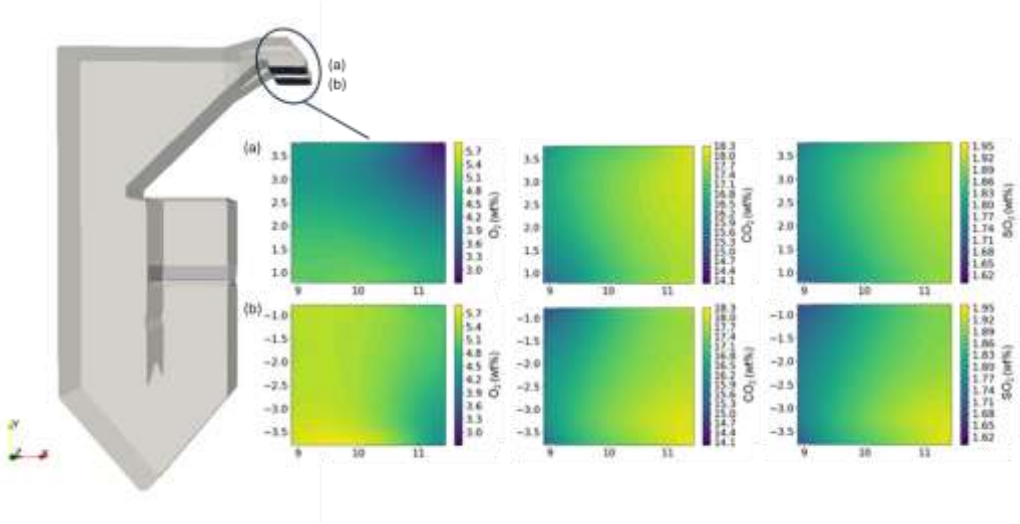

Figure 17. Dry wt% of CO_2, O_2 and SO_2 at the two outlet planes (**a**) and (**b**).

The O_2 content ranges between 2.8 and 5.8 wt%. Such variation across the outlet area indicates that the measurement depends highly on the position of the sensor. The deviation between measured and calculated O_2 content can therefore be partially attributed to the sensor position and partially to the simplified reaction system in the model.

Figure 18 shows the simulated mean particle mass loss over time as relative mass m/m_0.

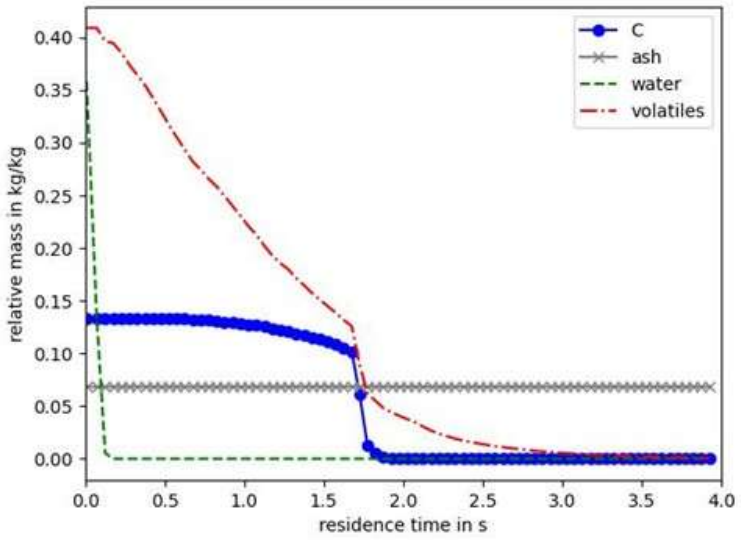

Figure 18. Mean relative particle mass m/m_0 in kg/kg over residence time for the experiment 2 mm, 30°, hollowcone.

The water content is depleted in less than 0.2 s. Char combustion begins when the residual coefficient of the volatiles is reached, peaks at around 1.7 s, and completes after around 1.9 s. Bajpai et al. provide the following timeframe for black liquor droplet combustion [2]:

- Drying 0.1–0.2 s;
- Devolatilization: 0.2–0.3 s;
- Char combustion: 0.5–1 s.

Järvinen determined the combustion time of 2 mm black liquor droplets in 1000 °C dry air experimentally [32]. The drying and devolatilization were completed after around 2.8 s and the char combustion after around 6 s. While these time frames are not specific to red liquor combustion, they indicate what to expect and show that our simulation results are in the expected range given in the literature.

The overall results show a satisfactory alignment with both industrial plant data and the literature. Considering that the objective of this study is a qualitative assessment evaluating the influence of spraying characteristics on combustion time rather than quantitative analyses, the simulations are evaluated as reliable for a comparative parameter study.

3.2. Effect of Spray Characteristics on Combustion Time

Figure 19 shows the simulated spraying behavior close to the nozzle.

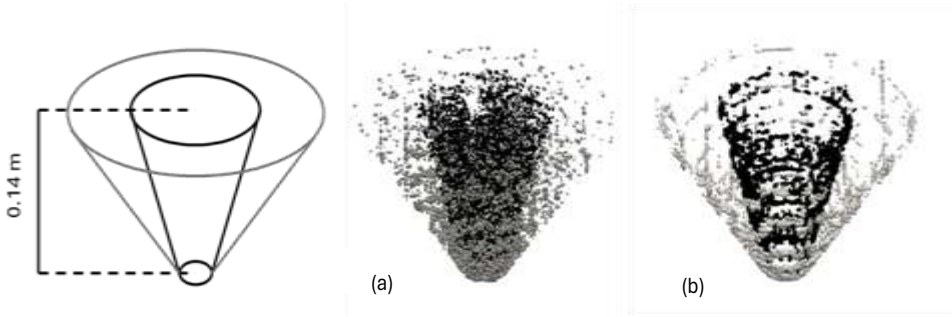

Figure 19. Simulated spray; 30° spray angle in grey, 15° spray angle in black; (**a**) fullcone; (**b**) hollowcone.

Figure 20 shows the mean combustion time for a particle for the different virtual experiments, and Table 8 gives the exact times in numbers. The combustion time is defined as the time when the char content in the particle reaches the threshold of 0.01. The reported combustion time corresponds to the mean of the individual parcel burnout times.

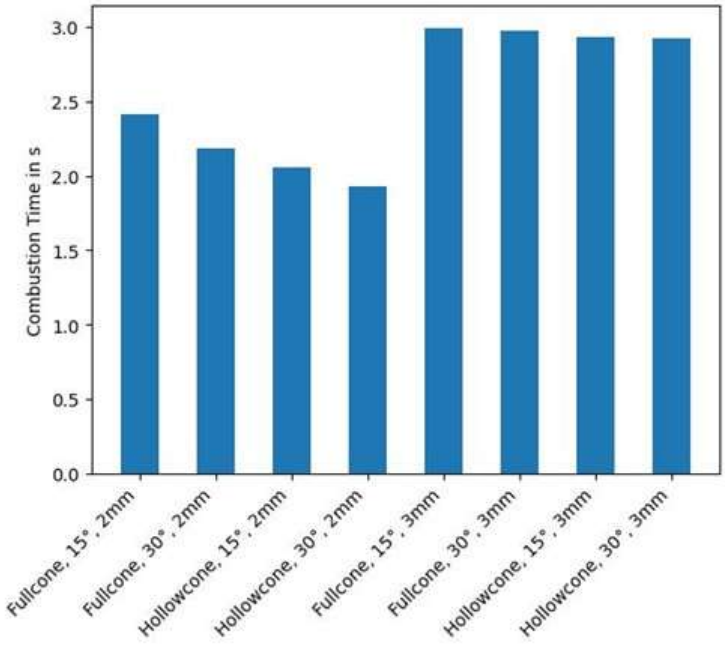

Figure 20. Mean combustion time for a particle for the different virtual experiments.

Table 8. Results of the design of virtual experiment.

Factor	Particle Size λ (mm)	Spraying Angle (°)	Spray Type	Combustion Time (s)
Experiment #1	2	30	Hollowcone	1.39
Experiment #2	2	15	Hollowcone	2.05
Experiment #3	3	30	Hollowcone	2.92
Experiment #4	3	15	Hollowcone	2.93
Experiment #5	2	30	Fullcone	2.18
Experiment #6	2	15	Fullcone	2.41
Experiment #7	3	30	Fullcone	2.97
Experiment #8	3	15	Fullcone	2.99

The fastest combustion is achieved when combusting particles with a characteristic particle size of 2 mm with hollowcone spraying and a spraying angle of 30°. Combusting particles with a characteristic particle size of 3 mm with fullcone spraying and a spray angle of 15° shows the longest combustion time. The following discusses the influence of the three investigated spraying characteristics (droplet size, spraying angle, and spray type) on the particle combustion time in detail.

3.2.1. Influence of Droplet Size

As expected, a smaller mean droplet diameter accelerates combustion due to reduced mass needing evaporation and devolatilization. Figure 21 illustrates this effect by comparing the mean particle mass loss over time across different experiments, with particle size being the sole distinguishing factor in each pair.

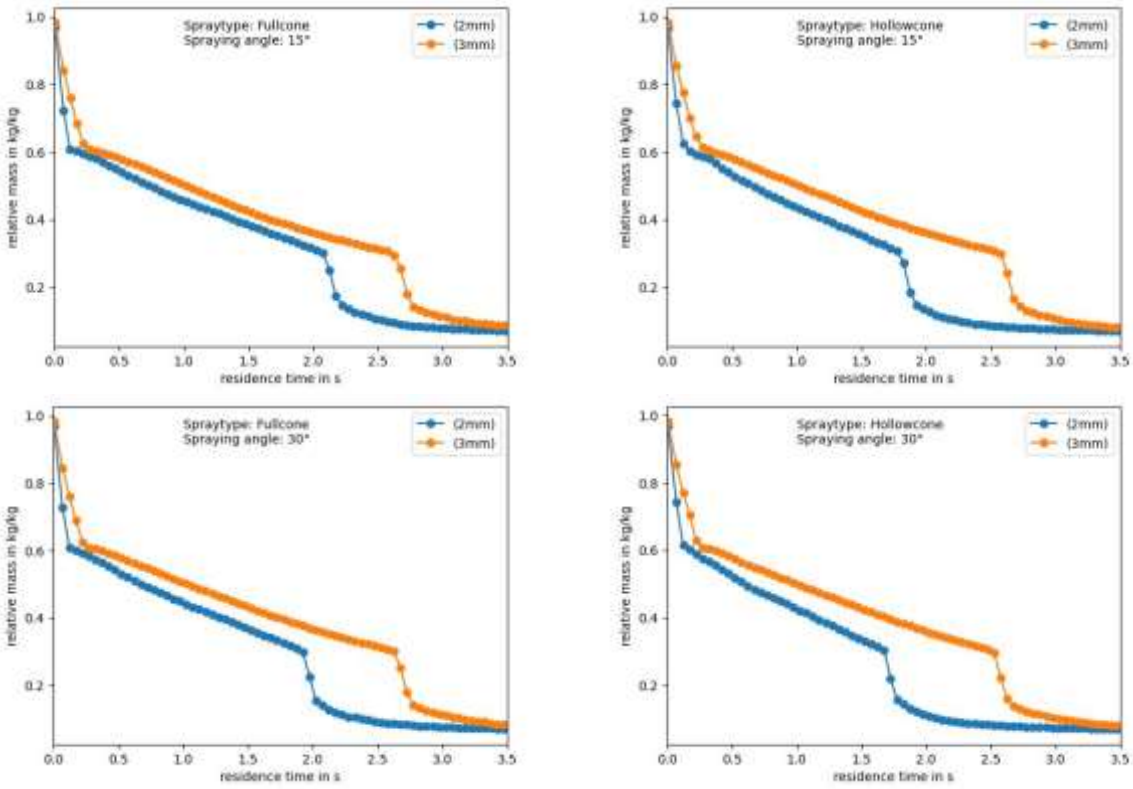

Figure 21. Mean particle mass as relative mass m/m_0 over time for mean droplet size 2 mm vs. 3 mm.

The initial drop in mass is attributed to drying, followed by a less steep mass loss due to devolatilization. The rapid decrease in mass loss indicates the main char combustion phase. Table 9 gives the calculated effect of particle diameter reduction on combustion time (CT) in %:

$$Effect\ of\ diameter\ reduction = \frac{CT_{2mm} - CT_{3mm}}{CT_{3mm}} \quad (29)$$

Table 9. Calculated influence of mean droplet size on particle combustion time.

Spraying Angle (°)	Spray Type	Effect of Particle Reduction (%)
15	Hollowcone	−30
30	Hollowcone	−34
15	Fullcone	−19
30	Fullcone	−27

The reduction in combustion time across all sets of experiments is ≥19%, highlighting the significant impact of particle size on combustion duration. When spraying as hollow-cone with a spraying angle of 30° the combustion time is 34% faster when reducing the characteristic particle size from 3 mm to 2 mm.

3.2.2. Influence of Spraying Angle

Figure 22 shows the mean particle mass loss over time across different experiments, with the spraying angle being the sole distinguishing factor in each pair.

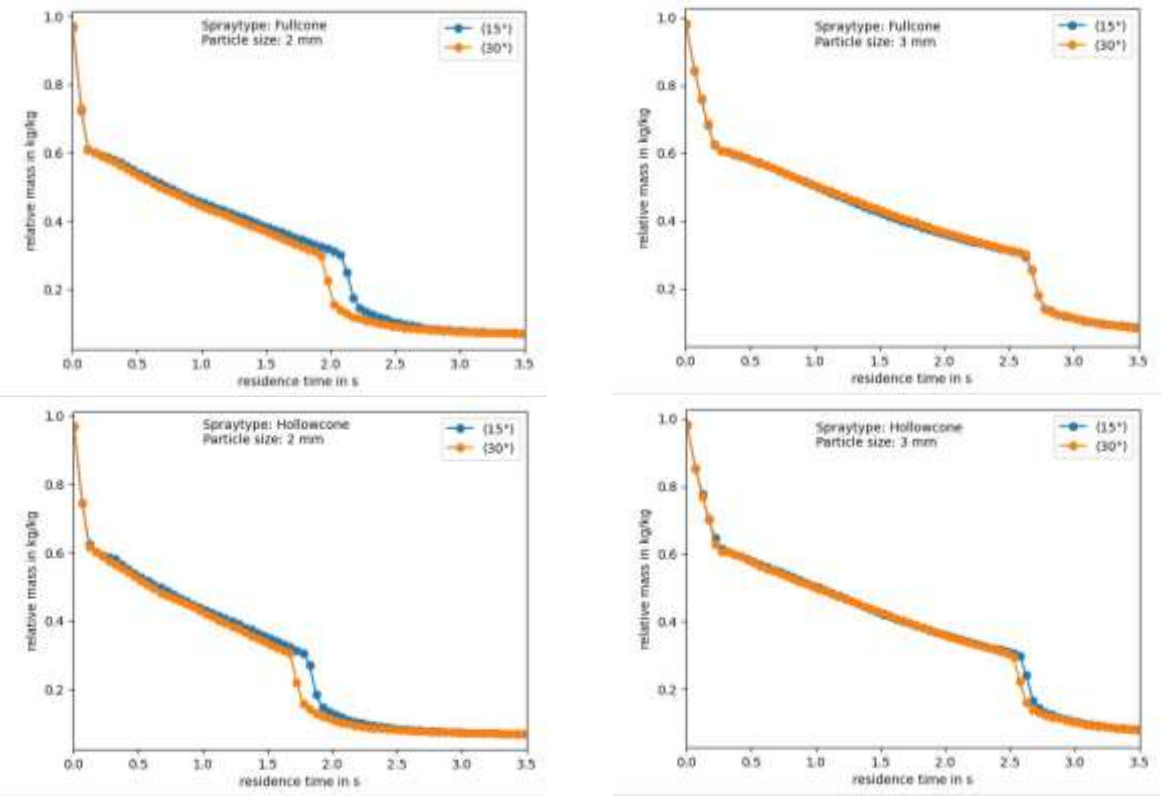

Figure 22. Mean particle mass as relative mass m/m$_0$ over time for spraying angle 15° vs 30°.

Almost all experiments show that widening the spraying angle accelerates combustion. When combusting particles with a characteristic size of 3 mm with fullcone spraying, no change in combustion time can be observed. Table 10 gives the calculated effect of widening the spraying angle on combustion time (CT) in %:

$$Effect\ of\ spraying\ angle = \frac{CT_{30°} - CT_{15°}}{CT_{30°}} \quad (30)$$

Table 10. Calculated influence of spraying angle on particle combustion time.

Particle Size λ (mm)	Spray Type	Effect of Widened Spraying Angle (%)
2	Hollowcone	−6
3	Hollowcone	0
2	Fullcone	−10
3	Fullcone	−1

When combusting 2 mm particles, the combustion time is reduced by up to 10% by using a 30° spray angle instead of a 15° spray angle. When combusting particles with a characteristic size of 3 mm, the effect is insignificant.

3.2.3. Influence of Spray Type

Figure 23 shows the mean particle mass loss over time across different experiments, with the spray type being the sole distinguishing factor in each pair.

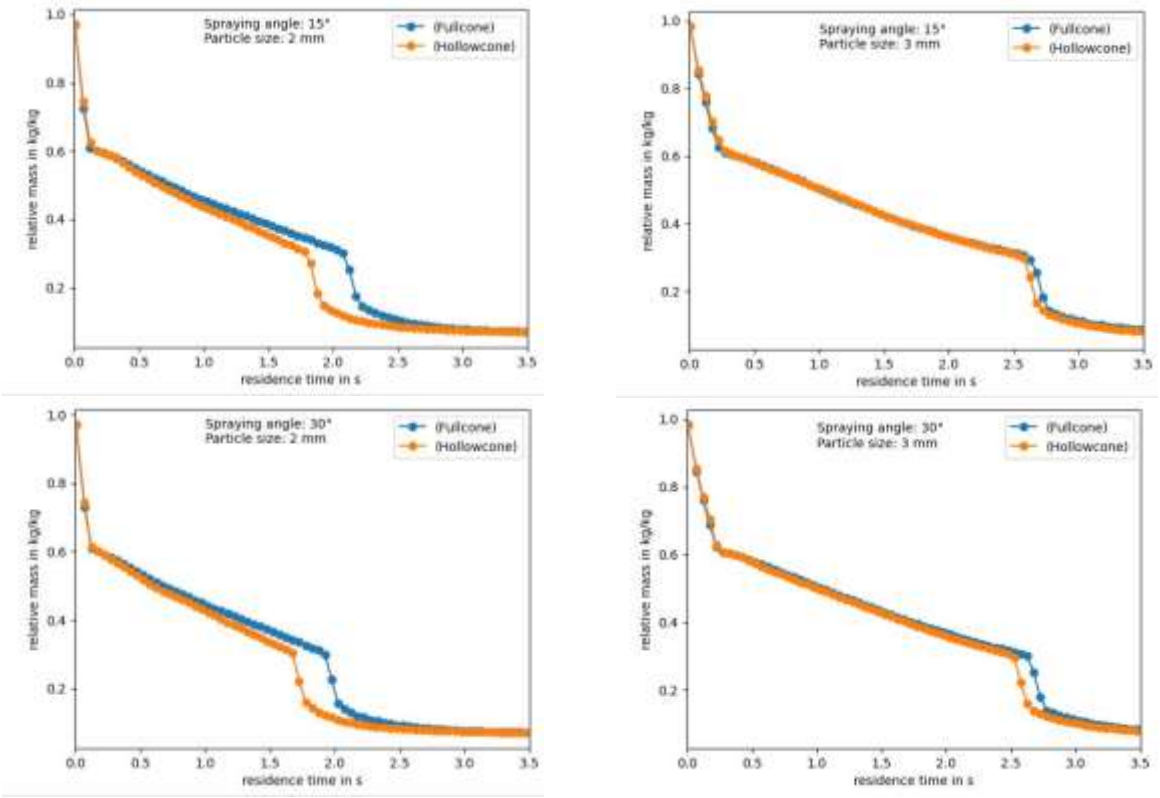

Figure 23. Mean particle mass as relative mass m/m$_0$ over time for spray type fullcone vs hollowcone.

For all cases, hollowcone spraying is beneficial for a fast combustion compared to fullcone spraying. Table 11 gives the calculated effect of changing the spray type on combustion time (CT) in %:

$$Effect\ of\ spray\ type = \frac{CT_{Hollowcone} - CT_{Fullcone}}{CT_{Fullcone}} \quad (31)$$

Table 11. Calculated influence of spray type on particle combustion time.

Particle Size λ (mm)	Spraying Angle (°)	Effect of Changing Spray Type (%)
2	15	−15
3	15	−2
2	30	−12
3	30	−2

For all experiments, changing the spray type from fullcone to hollowcone has a reducing effect on combustion time. The reduction in combustion time is with 12 and 15% high when combusting 2 mm particles, while the effect is with 2% significantly smaller when combusting 3 mm particles.

4. Conclusions and Outlook

A CFD model for the combustion of red liquor was developed, and CFD simulations were performed analyzing the effect of different spraying characteristics on the droplet combustion time inside an industrial-sized combustion vessel. The results demonstrate that our simulations align reasonably well with industrial plant data and literature sources. They also yield physically expected outcomes, affirming the reliability of our CFD setup for qualitative studies investigating the influence of various parameters on

combustion time. Through virtual experiments varying spraying characteristics such as characteristic particle size, spraying angle, and spray type, we discovered that the fastest combustion was achieved with a characteristic droplet size of 2 mm, a spraying angle of 30°, and using the hollowcone spray type. These spraying characteristics promote the best fuel dispersion within the combustion vessel, leading to accelerated combustion rates. Notably, reducing particle diameter exhibited the most significant effect, reducing combustion time by approximately 30%. Widening the spraying angle from 15° to 30° could further enhance combustion by up to 10% when combusting droplets with a characteristic size of 2 mm, although this effect was marginal when combusting droplets with a characteristic size of 3 mm. Similarly, switching from fullcone to hollowcone spraying reduced combustion time by up to 15% when combusting droplets with a characteristic size of 2 mm and 2% when combusting droplets with a characteristic size of 3 mm. Overall, the influence of spraying characteristics on combustion time was higher for fuel droplets with a characteristic size of 2 mm compared to fuel droplets with a characteristic size of 3 mm.

With our study, we aimed to perform a comparative study of the influence of different spraying characteristics on the combustion time. For that purpose, we implemented one-step combustion models and derived devolatilization and char combustion kinetics from single-heating-rate non-isothermal TG analyses. The derived kinetic parameters serve as a first approximation sufficient for the performed comparative assessment. For a rigorous determination of intrinsic kinetic parameters, it is recommended to follow the ICTAC recommendation to perform multi-heating-rate approaches. To improve the level of detail of the performed simulations, we recommend expanding the implemented reaction models into a sophisticated reaction system, including the H_2O and CO_2 gasification of char and the resolved description of the devolatilization of single components. It must be noted that such an extension requires detailed experimental kinetic determination. Furthermore, the model can be improved by incorporating particle swelling, a typical behavior of spent pulping liquor during combustion, and non-sphericity of the particles. The findings of this study highlight the potential that lies in optimizing spraying characteristics for improving combustion efficiency. Applicable measures to achieve an optimized fuel spray can range from straightforward implementations requiring no modification to the combustion vessel or nozzles—such as reducing fuel viscosity or optimizing the fuel-to-steam ratio in two-phase nozzles—to more advanced nozzle redesign, including the integration of optimized swirl bodies or related flow-enhancing geometries.

Author Contributions: Conceptualization, B.D.W., E.-M.W., C.J., T.L. and B.H.; methodology, B.D.W., E.-M.W. and C.J.; software, B.D.W., E.-M.W. and C.J.; validation, B.D.W. and E.-M.W.; formal analysis, B.D.W., E.-M.W. and C.J.; investigation, B.D.W., E.-M.W. and C.J.; resources, C.J., T.L. and M.H.; data curation, B.D.W.; writing—original draft preparation, B.D.W.; writing—review and editing, B.D.W., E.-M.W., C.J. and B.H.; visualization, B.D.W.; supervision, B.H. and M.H.; project administration, M.H.; funding acquisition, M.H. All authors have read and agreed to the published version of the manuscript.

Funding: This research was funded by the Austrian Research Promotion Agency (FFG), grant number FFG 868.615. The authors acknowledge TU Wien Bibliothek for financial support through its Open Access Funding Programme.

Data Availability Statement: The original contributions presented in this study are included in the article. Further inquiries can be directed to the corresponding author.

Acknowledgments: The authors acknowledge the support by the Competence Center CHASE GmbH. CHASE Competence Center is subsidized in the frame of COMET—Competence Centers for Excellent Technologies by BMVIT, BMWFW, Wirtschaftsagentur Wien, State of Upper Austria, and its scientific partners. The COMET program is handled by FFG. The authors especially thank

Karin Wieland from the Competence Center CHASE GmbH for her cooperation on the project. The support by the project partner Sappi Papier Holding GmbH is greatly acknowledged. The content of this paper was previously included in the author's dissertation thesis, which is publicly accessible through the TU Wien repository: Weiß, B. D.: Simulation and optimization of recovery systems in the pulp and paper industry, TU Wien, Vienna, Austria, 2024: "Open Access Funding by TU Wien".

Conflicts of Interest: Author Thomas Ladinek was employed by the company Sappi Austria Produktions-GmbH & Co. KG, which provided data for the conducted study. Author Bahram Haddadi was employed by the company Competence Center CHASE GmbH. The remaining authors declare no conflicts of interest. The funders had no role in the design of the study; in the collection, analyses, or interpretation of data; in the writing of the manuscript, or in the decision to publish the results.

Abbreviations and Symbols

The following abbreviations are used in this manuscript:

Abbreviations		
CFD		Computational Fluid Dynamics
CT		Combustion Time
PDF		Probability Density Function
TGA		Thermogravimetric Analysis
Roman symbols		
A	1/s	Pre-exponential factor
A_{void}	m²	Void area
A_{total}	m²	Total area
C_D	-	Drag coefficient
D	1/m²	Darcy coefficient
E	J/kmol	Activation Energy
F	1/m	Forchheimer coefficient
F_D	kg m/s²	Drag force
F_g	kg m/s²	Gravitational force
F_L	kg m/s²	Lift force
K	m²/s²	Kinetic energy
N	-	Random normal with mean 0 and standard deviation 1
Nu	-	Nusselt number
Pr	-	Prandtl number
R	J/(K kmol)	Universal gas constant
Re	-	Reynolds number
S_h	J/(m³s)	Energy source term
S_m	kg/(m³s)	Mass source term
S_u	N/(m³s)	Momentum source term
Sh	-	Sherwood number
Sc	-	Schmidt number
T	K	Temperature
T_{Devol}	K	Temperature at which devolatilization starts
U	m/s	Velocity
Y	kg/kg	Mass fraction
a	-	Random between 0 and 1
d	m	Diameter
d_v	-	Vector $[a\cos(\theta), a\sin(\theta), u]$.
$f_{x,y,z}$	-	Porosity
g	m/s²	Gravitational acceleration
h	J/kg	Enthalpy
k	m²/s²	Turbulent kinetic energy
k_{kin}	1/s	Kinetic rate
m	kg	Mass
n	-	Shape parameter in Rosin–Rammler (Weibull) PDF
p_i	kg/(m s²)	Partial pressure of component i

Δp	kg/(m s^2)	Pressure loss
t	s	Time
u	-	Random between −1 and 1
$\vec{u}$	m/s	Velocity vector
Greek symbols		
α_{eff}	m^2/s	Effective thermal diffusivity
ε	m^2/s^3	Turbulent dissipation rate
θ	-	Random between 0 and 2
λ	m	Characteristic particle size
μ	kg/(m s)	Dynamic viscosity
μ_{eff}	kg/(m s)	Effective viscosity
ρ	kg/m^3	Density
τ	kg/(m s^2)	Stress tensor
τ_{tur}	s	Turbulent timestep
ω	1/s	Vorticity
Subscripts		
∞		Far field
c		Centerline
F		Film around particle
g		Gas
i		Species i
m		Maximum
p		Particle

References

1. Bajpai, P. (Ed.) Chapter 1—Introduction. In *Pulp and Paper Industry: Chemical Recovery*; Elsevier: Amsterdam, The Netherlands, 2017; pp. 1–23. ISBN 978-0-12-811103-1.
2. Bajpai, P. (Ed.) Chapter 4—Combustion of Black Liquor. In *Pulp and Paper Industry: Energy Conservation*; Elsevier: Amsterdam, The Netherlands, 2016; pp. 67–100. ISBN 978-0-12-803411-8.
3. Lee, J.; Woo, S.; Lee, I.; Han, Y.; Yoon, Y. Characteristics of spray and combustion in gas-centered swirl coaxial injector with varying gas nozzle diameter. *Acta Astronaut.* **2024**, *215*, 631–641. https://doi.org/10.1016/j.actaastro.2023.12.044.
4. Gopinath, S.; Devan, P.K.; Sabarish, V.; Sabharish Babu, B.V.; Sakthivel, S.; Vignesh, P. Effect of spray characteristics influences combustion in DI diesel engine—A review. *Mater. Today Proc.* **2020**, *33*, 52–65. https://doi.org/10.1016/j.matpr.2020.03.130.
5. Zhao, Y.; Fan, W.; Zhang, R. Experimental study on the effect of injection schemes on fuel spray and combustion characteristics in a compact combustor. *Aerosp. Sci. Technol.* **2023**, *141*, 108510. https://doi.org/10.1016/j.ast.2023.108510.
6. Intergovernmental Panel on Climate Change (IPCC) (Ed.) *Climate Change 2022: Mitigation of Climate Change: Working Group III Contribution to the Sixth Assessment Report of the Intergovernmental Panel on Climate Change*; Cambridge University Press: Cambridge, UK; New York, NY, USA, 2022; pp. 1161–1244. ISBN 9781009157926.
7. Del Rio, D.D.F.; Sovacool, B.K.; Griffiths, S.; Bazilian, M.; Kim, J.; Foley, A.M.; Rooney, D. Decarbonizing the pulp and paper industry: A critical and systematic review of sociotechnical developments and policy options. *Renew. Sustain. Energy Rev.* **2022**, *167*, 112706. https://doi.org/10.1016/j.rser.2022.112706.
8. Horton, R.R.; Grace, T.M.; Adams, T.N. The effects of black liquor spray parameters on combustion behavior in recovery furnace simulations. In Proceedings of the International Recovery Conference, Seattle, WA, USA, 7–11 June 1992.
9. Laitinen, A.; Laurila, E.; Keskinen, K.; Vuorinen, V. Large-Eddy Simulation of two secondary air supply strategies in kraft recovery boilers. *Appl. Therm. Eng.* **2022**, *216*, 119035. https://doi.org/10.1016/j.applthermaleng.2022.119035.
10. Shinjo, J. Recent Advances in Computational Modeling of Primary Atomization of Liquid Fuel Sprays. *Energies* **2018**, *11*, 2971. https://doi.org/10.3390/en11112971.
11. Hirche, D.; Birkholz, F.; Hinrichsen, O. A hybrid Eulerian-Eulerian-Lagrangian model for gas-solid simulations. *Chem. Eng. J.* **2019**, *377*, 119743. https://doi.org/10.1016/j.cej.2018.08.129.
12. Tahry, S.H.E. k-epsilon equation for compressible reciprocating engine flows. *J. Energy* **1983**, *7*, 345–353. https://doi.org/10.2514/3.48086.
13. Launder, B.E.; Spalding, D.B. The numerical computation of turbulent flows. *Comput. Methods Appl. Mech. Eng.* **1974**, *3*, 269–289. https://doi.org/10.1016/0045-7825(74)90029-2.

14. Wartha, E.-M.; Haugen, N.E.; Karchniwy, E.; Bösenhofer, M.; Harasek, M.; Løvås, T. The effect of turbulence on the conversion of coal under blast furnace raceway conditions. *Fuel* **2023**, *331*, 125840. https://doi.org/10.1016/j.fuel.2022.125840.
15. Bösenhofer, M.; Wartha, E.-M.; Jordan, C.; Harasek, M. The Eddy Dissipation Concept—Analysis of Different Fine Structure Treatments for Classical Combustion. *Energies* **2018**, *11*, 1902. https://doi.org/10.3390/en11071902.
16. Sazhin, S.S.; Sazhina, E.M.; Faltsi-Saravelou, O.; Wild, P. The P-1 model for thermal radiation transfer: Advantages and limitations. *Fuel* **1996**, *75*, 289–294. https://doi.org/10.1016/0016-2361(95)00269-3.
17. Putnam, A. Integratable form of droplet drag coefficient. *ARS J.* **1961**, *31*, 1467–1468.
18. Mei, R. An approximate expression for the shear lift force on a spherical particle at finite reynolds number. *Int. J. Multiph. Flow* **1992**, *18*, 145–147. https://doi.org/10.1016/0301-9322(92)90012-6.
19. P. Saffman. The lift on a small sphere in a slow shear flow. *J. Fluid Mech.* **1965**, *22*, 385–400.
20. Gosman, A.; Ioannides, E. Aspects of computer simulation of liquid-fuelled combustors. In *Proceedings of the 19th Aerospace Sciences Meeting, St. Louis, MO, USA, 12–15 January 1981*; American Institute of Aeronautics and Astronautics: Reston, VA, USA, 1983; p. 01121981.
21. Ranz, W.; Marshall, W.R.J. Evaporation from drops: Part I. *Chem. Eng. Prog.* **1952**, *48*, 141–146.
22. Singh, S.P.; Bansal, M.C. Combustion kinetics for soda black liquor-bagasse pith. *Energy Sources Part A Recovery Util. Environ. Eff.* **2016**, *38*, 1197–1205. https://doi.org/10.1080/15567036.2014.899409.
23. Järvinen, M.; Zevenhoven, R.; Vakkilainen, E.; Forssén, M. Black liquor devolatilization and swelling—A detailed droplet model and experimental validation. *Biomass Bioenergy* **2003**, *24*, 495–509. https://doi.org/10.1016/S0961-9534(02)00151-4.
24. Spalding, D.B. The combustion of liquid fuels. *Symp. Int. Combust.* **1953**, *4*, 847–864. https://doi.org/10.1016/S0082-0784(53)80110-4.
25. Sanchez, P.S. *Modeling the Dispersion and Evaporation of Sprays in Aero-Nautical Combustion Chambers*; Institut National Polytechnique de Toulouse—INPT: Toulouse, France, 2012.
26. Zuo, B.; Gomes, A.M.; Rutland, C.J. Studies of Superheated Fuel Spray Structures and Vaporization in GDI engines. In Proceedings of the Eleventh International Multidimensional Engine Modeling User's Group Meeting, Detroit, MI, USA, 4 March 2001.
27. Magnussen, B.F.; Hjertager, B.H. On mathematical modeling of turbulent combustion with special emphasis on soot formation and combustion. *Symp. Int. Combust.* **1977**, *16*, 719–729. https://doi.org/10.1016/S0082-0784(77)80366-4.
28. Wartha, E.-M.; Bösenhofer, M.; Harasek, M. Characteristic Chemical Time Scales for Reactive Flow Modeling. *Combust. Sci. Technol.* **2021**, *193*, 2807–2832. https://doi.org/10.1080/00102202.2020.1760257.
29. Idelchik, I.E. *Handbook of Hydraulic Resistance*, 3rd ed.; Begell House: Danbury, CT, USA, 1994; 790p. ISBN 0-8493-9908-4.
30. Mi, J.; Kalt, P.; Nathan, G.J. Near-Field Mixing Characteristics of Turbulent Jet Issuing from a Notched-Rectangular Orifice Plate. In *New Trends in Fluid Mechanics Research: Proceedings of the Fifth International Conference on Fluid Mechanics (Shanghai, 2007)*; Zhuang, F.G., Li, J.-C., Eds.; Tsinghua University Press: Beijing, China; Springer: Berlin/Heidelberg, Germany, 2008; pp. 162–165. ISBN 978-3-540-75995-9.
31. Crrnin, F. *Truncated Weibull Distribution Functions and Moments*; SSRN: New York, NY, USA, 2015.
32. Järvinen, M.P. Numerical Modeling of the Drying, Devolatilization and Char Conversion Processes of Black Liquor Droplets. Ph.D. Thesis, Helsinki University of Technology, Espoo, Finland, 2002.